In Vivo Imaging of Cerebral Energy Metabolism with Two-Photon Fluorescence Lifetime Microscopy of NADH

Biomedical Optics EXPRESS

In vivo imaging of cerebral energy metabolism with two-photon fluorescence lifetime microscopy of NADH

Mohammad A. Yaseen,[1] Sava Sakadžić,[1] Weicheng Wu,[1] Wolfgang Becker,[2] Karl A. Kasischke,[3] and David A. Boas[1,*]

[1]*Optics Division, MGH/MIT/HMS Athinoula A. Martinos Center for Biomedical Imaging, Massachusetts General Hospital/Harvard Medical School, Charlestown, Massachusetts 02129, USA*
[2]*Becker & Hickl GmbH, Nahmitzer Damm 30, 12277 Berlin, Germany*
[3]*Department of Neurology, University of Ulm Medical Center, Oberer Eselsberg 45, 89075 Ulm, Germany*
[*]*dboas@nmr.mgh.harvard.edu*

Abstract: Minimally invasive, specific measurement of cellular energy metabolism is crucial for understanding cerebral pathophysiology. Here, we present high-resolution, *in vivo* observations of autofluorescence lifetime as a biomarker of cerebral energy metabolism in exposed rat cortices. We describe a customized two-photon imaging system with time correlated single photon counting detection and specialized software for modeling multiple-component fits of fluorescence decay and monitoring their transient behaviors. *In vivo* cerebral NADH fluorescence suggests the presence of four distinct components, which respond differently to brief periods of anoxia and likely indicate different enzymatic formulations. Individual components show potential as indicators of specific molecular pathways involved in oxidative metabolism.

OCIS codes: (170.0170) Medical optics and biotechnology; (180.4315) Nonlinear microscopy; (170.3650) Lifetime-based sensing.

References and Links

1. L. Sokoloff, "The physiological and biochemical bases of functional brain imaging," Cogn Neurodyn **2**(1), 1–5 (2008).
2. D. C. Wallace, "A mitochondrial paradigm of metabolic and degenerative diseases, aging, and cancer: a dawn for evolutionary medicine," Annu. Rev. Genet. **39**(1), 359–407 (2005).
3. M. Monsalve, S. Borniquel, I. Valle, and S. Lamas, "Mitochondrial dysfunction in human pathologies," Front. Biosci. **12**(1), 1131–1153 (2007).
4. M. R. Duchen, "Mitochondria in health and disease: perspectives on a new mitochondrial biology," Mol. Aspects Med. **25**(4), 365–451 (2004).
5. F. Hyder, "Dynamic imaging of brain function," in *Dynamic Brain Imaging: Multi-Modal Methods and In vivo Applications*, F. Hyder, ed. (Humana, Totowa, NJ, 2009), pp. 3–21.
6. B. Chance, P. Cohen, F. Jobsis, and B. Schoener, "Intracellular oxidation-reduction states *in vivo*: the microfluorometry of pyridine nucleotide gives a continuous measurement of the oxidation state," Science **137**(3529), 499–508 (1962).
7. A. A. Heikal, "Intracellular coenzymes as natural biomarkers for metabolic activities and mitochondrial anomalies," Biomarkers Med. **4**(2), 241–263 (2010).
8. B. Chance and B. Thorell, "Localization and kinetics of reduced pyridine nucleotide in living cells by microfluorometry," J. Biol. Chem. **234**, 3044–3050 (1959).
9. K. Svoboda and R. Yasuda, "Principles of two-photon excitation microscopy and its applications to neuroscience," Neuron **50**(6), 823–839 (2006).
10. G. H. Patterson, S. M. Knobel, P. Arkhammar, O. Thastrup, and D. W. Piston, "Separation of the glucose-stimulated cytoplasmic and mitochondrial NAD(P)H responses in pancreatic islet β cells," Proc. Natl. Acad. Sci. U.S.A. **97**(10), 5203–5207 (2000).
11. S. Huang, A. A. Heikal, and W. W. Webb, "Two-photon fluorescence spectroscopy and microscopy of NAD(P)H and flavoprotein," Biophys. J. **82**(5), 2811–2825 (2002).

#179359 - $15.00 USD Received 6 Nov 2012; revised 17 Jan 2013; accepted 17 Jan 2013; published 22 Jan 2013

12. W. R. Zipfel, R. M. Williams, R. Christie, A. Y. Nikitin, B. T. Hyman, and W. W. Webb, "Live tissue intrinsic emission microscopy using multiphoton-excited native fluorescence and second harmonic generation," Proc. Natl. Acad. Sci. U.S.A. **100**(12), 7075–7080 (2003).
13. K. A. Kasischke, H. D. Vishwasrao, P. J. Fisher, W. R. Zipfel, and W. W. Webb, "Neural activity triggers neuronal oxidative metabolism followed by astrocytic glycolysis," Science **305**(5680), 99–103 (2004).
14. W. Becker, *Advanced Time-Correlated Single Photon Counting Techniques* (Springer, Berlin, 2005).
15. M. Y. Berezin and S. Achilefu, "Fluorescence lifetime measurements and biological imaging," Chem. Rev. **110**(5), 2641–2684 (2010).
16. J. R. Lakowicz, *Principles of Fluorescence Spectroscopy* (Springer, New York, 2006).
17. D. F. Eaton, "Recommended methods for fluorescence decay analysis," Pure Appl. Chem. **62**(8), 1631–1648 (1990).
18. R. Niesner, B. Peker, P. Schlüsche, and K.-H. Gericke, "Noniterative biexponential fluorescence lifetime imaging in the investigation of cellular metabolism by means of NAD(P)H autofluorescence," ChemPhysChem **5**(8), 1141–1149 (2004).
19. H. D. Vishwasrao, A. A. Heikal, K. A. Kasischke, and W. W. Webb, "Conformational dependence of intracellular NADH on metabolic state revealed by associated fluorescence anisotropy," J. Biol. Chem. **280**(26), 25119–25126 (2005).
20. Q. Yu and A. A. Heikal, "Two-photon autofluorescence dynamics imaging reveals sensitivity of intracellular NADH concentration and conformation to cell physiology at the single-cell level," J. Photochem. Photobiol. B **95**(1), 46–57 (2009).
21. T. H. Chia, A. Williamson, D. D. Spencer, and M. J. Levene, "Multiphoton fluorescence lifetime imaging of intrinsic fluorescence in human and rat brain tissue reveals spatially distinct NADH binding," Opt. Express **16**(6), 4237–4249 (2008).
22. M. C. Skala, K. M. Riching, A. Gendron-Fitzpatrick, J. Eickhoff, K. W. Eliceiri, J. G. White, and N. Ramanujam, "*In vivo* multiphoton microscopy of NADH and FAD redox states, fluorescence lifetimes, and cellular morphology in precancerous epithelia," Proc. Natl. Acad. Sci. U.S.A. **104**(49), 19494–19499 (2007).
23. C. Stringari, A. Cinquin, O. Cinquin, M. A. Digman, P. J. Donovan, and E. Gratton, "Phasor approach to fluorescence lifetime microscopy distinguishes different metabolic states of germ cells in a live tissue," Proc. Natl. Acad. Sci. U.S.A. **108**(33), 13582–13587 (2011).
24. S. Sakadžić, E. Roussakis, M. A. Yaseen, E. T. Mandeville, V. J. Srinivasan, K. Arai, S. Ruvinskaya, A. Devor, E. H. Lo, S. A. Vinogradov, and D. A. Boas, "Two-photon high-resolution measurement of partial pressure of oxygen in cerebral vasculature and tissue," Nat. Methods **7**(9), 755–759 (2010).
25. M. A. Yaseen, V. J. Srinivasan, S. Sakadžić, H. Radhakrishnan, I. Gorczynska, W. Wu, J. G. Fujimoto, and D. A. Boas, "Microvascular oxygen tension and flow measurements in rodent cerebral cortex during baseline conditions and functional activation," J. Cereb. Blood Flow Metab. **31**(4), 1051–1063 (2011).
26. L. K. Klaidman, A. C. Leung, and J. D. Adams, Jr., "High-performance liquid chromatography analysis of oxidized and reduced pyridine dinucleotides in specific brain regions," Anal. Biochem. **228**(2), 312–317 (1995).
27. R. Guarneri and V. Bonavita, "Nicotinamide adenine dinucleotides in the developing rat brain," Brain Res. **2**(2), 145–150 (1966).
28. Y. Avi-Dor, J. M. Olson, M. D. Doherty, and N. O. Kaplan, "Fluorescence of pyridine nucleotides in mitochondria," J. Biol. Chem. **237**, 2377–2383 (1962).
29. V. V. Ghukasyan and F.-J. Kao, "Monitoring cellular metabolism with fluorescence lifetime of reduced nicotinamide adenine dinucleotide," J. Phys. Chem. C **113**(27), 11532–11540 (2009).
30. E. Gratton, S. Breusegem, J. Sutin, Q. Ruan, and N. Barry, "Fluorescence lifetime imaging for the two-photon microscope: time-domain and frequency-domain methods," J. Biomed. Opt. **8**(3), 381–390 (2003).
31. M. Van Den Zegel, N. Boens, D. Daems, and F. C. De Schryver, "Possibilities and limitations of the time-correlated single photon counting technique: a comparative study of correction methods for the wavelength dependence of the instrument response function," Chem. Phys. **101**(2), 311–335 (1986).
32. A. Habenicht, J. Hjelm, E. Mukhtar, F. Bergström, and L. B.-Å. Johansson, "Two-photon excitation and time-resolved fluorescence: I. The proper response function for analysing single-photon counting experiments," Chem. Phys. Lett. **354**(5-6), 367–375 (2002).
33. K. Blinova, S. Carroll, S. Bose, A. V. Smirnov, J. J. Harvey, J. R. Knutson, and R. S. Balaban, "Distribution of mitochondrial NADH fluorescence lifetimes: steady-state kinetics of matrix NADH interactions," Biochemistry **44**(7), 2585–2594 (2005).
34. E. Baraghis, A. Devor, Q. Fang, V. J. Srinivasan, W. Wu, F. Lesage, C. Ayata, K. A. Kasischke, D. A. Boas, and S. Sakadzić, "Two-photon microscopy of cortical NADH fluorescence intensity changes: correcting contamination from the hemodynamic response," J. Biomed. Opt. **16**(10), 106003 (2011).
35. A. Nimmerjahn, F. Kirchhoff, J. N. D. Kerr, and F. Helmchen, "Sulforhodamine 101 as a specific marker of astroglia in the neocortex *in vivo*," Nat. Methods **1**(1), 31–37 (2004).
36. A. Gafni and L. Brand, "Fluorescence decay studies of reduced nicotinamide adenine dinucleotide in solution and bound to liver alcohol dehydrogenase," Biochemistry **15**(15), 3165–3171 (1976).
37. M. Wakita, G. Nishimura, and M. Tamura, "Some characteristics of the fluorescence lifetime of reduced pyridine nucleotides in isolated mitochondria, isolated hepatocytes, and perfused rat liver *in situ*," J. Biochem. **118**(6), 1151–1160 (1995).

#179359 - $15.00 USD Received 6 Nov 2012; revised 17 Jan 2013; accepted 17 Jan 2013; published 22 Jan 2013

38. T. G. Scott, R. D. Spencer, N. J. Leonard, and G. Weber, "Synthetic spectroscopic models related to coenzymes and base pairs. V. Emission properties of NADH. Studies of fluorescence lifetimes and quantum efficiencies of NADH, AcPyADH, [reduced acetylpyridineadenine dinucleotide] and simplified synthetic models," J. Am. Chem. Soc. **92**(3), 687–695 (1970).
39. D. K. Bird, L. Yan, K. M. Vrotsos, K. W. Eliceiri, E. M. Vaughan, P. J. Keely, J. G. White, and N. Ramanujam, "Metabolic mapping of MCF10A human breast cells via multiphoton fluorescence lifetime imaging of the coenzyme NADH," Cancer Res. **65**(19), 8766–8773 (2005).
40. V. K. Ramanujan, J. A. Jo, G. Cantu, and B. A. Herman, "Spatially resolved fluorescence lifetime mapping of enzyme kinetics in living cells," J. Microsc. **230**(3), 329–338 (2008).
41. D. Li, W. Zheng, and J. Y. Qu, "Time-resolved spectroscopic imaging reveals the fundamentals of cellular NADH fluorescence," Opt. Lett. **33**(20), 2365–2367 (2008).
42. M. W. Conklin, P. P. Provenzano, K. W. Eliceiri, R. Sullivan, and P. J. Keely, "Fluorescence lifetime imaging of endogenous fluorophores in histopathology sections reveals differences between normal and tumor epithelium in carcinoma in situ of the breast," Cell Biochem. Biophys. **53**(3), 145–157 (2009).
43. Y. Sun, J. Phipps, D. S. Elson, H. Stoy, S. Tinling, J. Meier, B. Poirier, F. S. Chuang, D. G. Farwell, and L. Marcu, "Fluorescence lifetime imaging microscopy: *in vivo* application to diagnosis of oral carcinoma," Opt. Lett. **34**(13), 2081–2083 (2009).
44. C. A. Thorling, X. Liu, F. J. Burczynski, L. M. Fletcher, G. C. Gobe, and M. S. Roberts, "Multiphoton microscopy can visualize zonal damage and decreased cellular metabolic activity in hepatic ischemia-reperfusion injury in rats," J. Biomed. Opt. **16**(11), 116011 (2011).
45. D. L. Nelson and M. M. Cox, *Lehninger Principles of Biochemistry* (W.H. Freeman, New York, 2008).
46. A. Devor, S. Sakadžić, P. A. Saisan, M. A. Yaseen, E. Roussakis, V. J. Srinivasan, S. A. Vinogradov, B. R. Rosen, R. B. Buxton, A. M. Dale, and D. A. Boas, "'Overshoot' of O_2 is required to maintain baseline tissue oxygenation at locations distal to blood vessels," J. Neurosci. **31**(38), 13676–13681 (2011).
47. B. Chance, B. Schoener, R. Oshino, F. Itshak, and Y. Nakase, "Oxidation-reduction ratio studies of mitochondria in freeze-trapped samples. NADH and flavoprotein fluorescence signals," J. Biol. Chem. **254**(11), 4764–4771 (1979).
48. N. D. Kirkpatrick, C. Zou, M. A. Brewer, W. R. Brands, R. A. Drezek, and U. Utzinger, "Endogenous fluorescence spectroscopy of cell suspensions for chemopreventive drug monitoring," Photochem. Photobiol. **81**(1), 125–134 (2005).
49. T. A. Wang, Y. V. Yu, G. Govindaiah, X. Ye, L. Artinian, T. P. Coleman, J. V. Sweedler, C. L. Cox, and M. U. Gillette, "Circadian rhythm of redox state regulates excitability in suprachiasmatic nucleus neurons," Science **337**(6096), 839–842 (2012).
50. S. K. Shankar, "Biology of aging brain," Indian J. Pathol. Microbiol. **53**(4), 595–604 (2010).
51. J. V. Rocheleau, W. S. Head, and D. W. Piston, "Quantitative NAD(P)H/flavoprotein autofluorescence imaging reveals metabolic mechanisms of pancreatic islet pyruvate response," J. Biol. Chem. **279**(30), 31780–31787 (2004).
52. J. R. Lakowicz, ed., *Principles of Fluorescence Spectroscopy* (Springer, New York, 2006).
53. M. vandeVen, M. Ameloot, B. Valeur, and N. Boens, "Pitfalls and their remedies in time-resolved fluorescence spectroscopy and microscopy," J. Fluoresc. **15**(3), 377–413 (2005).
54. M. Köllner and J. Wolfrum, "How many photons are necessary for fluorescence-lifetime measurements?" Chem. Phys. Lett. **200**(1-2), 199–204 (1992).

1. Introduction

Identifying and characterizing the complex cellular and molecular mechanisms of cerebral energy metabolism is critical to better understand brain function and its pathological alterations [1]. In order to accurately interpret the noninvasive, macroscopic observations of cerebral oxygenation and blood flow obtained by functional neuroimaging techniques such as positron emission tomography (PET) and functional magnetic resonance imaging (fMRI), more comprehensive insight into metabolic activity at a cellular level is crucial. Additionally, alterations in mitochondrial activity play a significant role in the aging process and the progression of stroke, cancer, and neurodegenerative diseases such as Alzheimer's Disease [2–4]. Monitoring these alterations could be useful as a biomarker for characterizing disease progression or determining the efficacy of novel therapies. Demand is therefore high to develop robust tools for monitoring metabolic activity with high spatial and temporal resolution *in vivo*, in which the complex interactions between neurons, astrocytes, and cerebral vasculature remain preserved [5]. Reduced nicotinamide adenine dinucleotide (NADH) is the ubiquitous electron carrier that plays crucial roles in both glycolysis and oxidative metabolism, and monitoring its autofluorescence has proven useful as a minimally invasive indicator of metabolic activity for ~50 years [6–8]. With absorption and emission

#179359 - $15.00 USD Received 6 Nov 2012; revised 17 Jan 2013; accepted 17 Jan 2013; published 22 Jan 2013

peaks in the UV region, the utility of monitoring NADH in scattering tissue samples with high resolution remained limited until the development of 2-Photon (2P) microscopy-based techniques, which capitalize on the spatially confined nonlinear excitation effect and the deep penetrating nature of near infrared excitation light [9–13]. More recent methods have coupled 2P microscopy with time-resolved fluorescence lifetime imaging microscopy (FLIM), extending the utility and specificity of NADH autofluorescence measurement to better characterize microenvironmental conditions around the fluorophore [14–17]. Using time-correlated single photon counting (TCSPC) methods, novel FLIM and anisotropy studies of NADH model its fluorescence decay as the sum of two or more decaying exponentials, with each term reportedly representing a different enzymatic bound formulation, or "specie" [18,19], of NADH. These species ostensibly could be more specific biomarkers of molecular pathways associated with glycolysis or oxidative phosphorylation [18–23], but more extensive characterization is required. Here, we describe 2P- FLIM based *in vivo* observations of cerebral NADH in the cortices of anesthetized rats using a customized imaging system and analysis software. We observed four distinct cerebral NADH species under physiological conditions with high spatial resolution, and we monitored transient alterations in the relative amounts of these species under anoxic conditions with relatively high temporal resolution.

2. Methods

2.1. Customized imaging system

Figure 1a depicts the 2P FLIM portion of our multimodal microscope [24,25], custom-designed for *in vivo* investigations of cerebral metabolism in small animals. Excitation is provided by a tunable Ti:sapphire laser (Mai Tai, Spectra Physics), delivering ~360 fs pulses after the objective at 80 MHz and tuned to $\lambda = 740$ nm. The excitation intensity is modulated with an electro-optic modulator (ConOptics, Danbury CT), raster-scanned across a field of view (FOV) ranging between 75 and 300 μm using galvanometer-based scanner mirrors (Cambridge Technology, Inc), and focused on the sample by a water immersion objective (Olympus XLumPlan Fluor, 20X, 1.00 NA, 2 mm working distance). Using a series of dichroic and bandpass filters, emitted light is spectrally separated and detected by a custom-designed four-channel detector array with high collection efficiency using photomultiplier tubes (PMTs) (Channel 1: 680 ± 30 nm, Channel 2: 595 ± 25 nm, Channel 3: 525 ± 25 nm, Channel 4: 460 ± 30 nm). NADH fluorescence is collected in channel 4 by a novel hybrid PMT with high detection efficiency and minimal afterpulsing (HPM-100-40 Becker & Hickl GmbH). As detailed in Subsection 2.4, fluorescence signal of the exogenous dye sulfurhodamine 101 (SR101) was detected in channel 2 simultaneously with the NADH collection. The SR101 intensity was used to co-register the NADH image with cellular structures and to correct for absorption changes associated with altered cerebral blood flow during physiological manipulations.

For FLIM investigations described herein, scanning and data collection were performed using commercial time-correlated single photon counting (TCSPC) hardware (SPC-150, GVD-120, DCC-100, Becker & Hickl GmbH) and control software (SPCM, Becker & Hickl GmbH).

NADH autofluorescence is spectrally identical to that of nicotinamide adenine dinucleotide phosphate (NADPH). In principle, the detected autofluorescence could arise from a mix of both NADH and NADPH. In metabolically active brain tissue, however, NADPH is widely believed to contribute minimally to the fluorescence signal, due to its much lower concentration in brain tissue [26,27], low quantum yield [28], and insensitivity to metabolic perturbation [13,19,29].

#179359 - $15.00 USD Received 6 Nov 2012; revised 17 Jan 2013; accepted 17 Jan 2013; published 22 Jan 2013

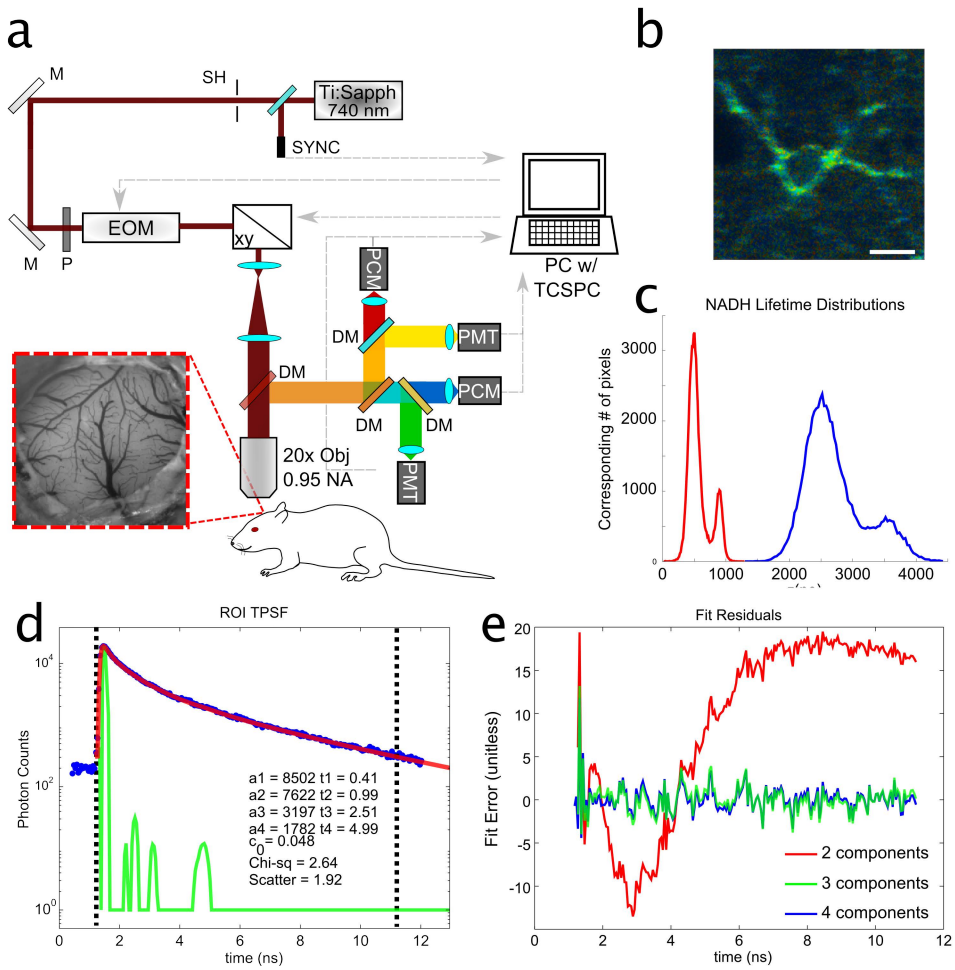

Fig. 1. (a) 2-photon imaging portion of our custom built *in vivo* imaging system, modified for FLIM measurements. SH: shutter, M: reflecting mirror, P: polarizer, EOM: electro-optic modulator, XY: galvanometer-based scanners, DM: Dichroic Mirror, PCM: photon counting module, PMT: photomultiplier tube. (a) Inset: reflectance image of the sealed cranial window model, approximately 3 mm in diameter at 570 nm. (b) *In vivo* image of NADH autofluorescence in a cortical astrocyte (Scale bar: 10 µm), with (c) pixel-wide distribution of 2-component fit performed with commercial SPCImage software, clearly showing 4 distinct peaks. (d) Example 4-component lifetime fit of *in vivo* cortical NADH fluorescence decay, computed with custom software. Blue profile: Collected, binned photon counts, Black-dashed lines: fitting boundaries, Green profile: computed IRF, Red profile: Computed decay profile (e) residuals for computed 2-, 3-, and 4-component lifetime fits to the example *in vivo* lifetime data, with reduced χ^2 errors of 195.16, 2.64, and 2.54, respectively.

2.2. Imaging protocol

High resolution (256 x 256 pixels) images were first acquired under baseline physiological conditions using $\Delta t \approx 50$ ps binning intervals and 256 temporal channels (12.8 ns-long decay profiles) over a field of view (FOV) ranging from 75 to 200 µm. Excitation intensity was adjusted to yield photon count rates of approximately 500,000 counts per second for these measurements, as indicated by the count rates continuously displayed in the SPCM software. Although incident power varied with cortical depth, it remained well below 50 mW for all measurements. For a given baseline measurement, such as the one provided in Fig. 1b, a repetitive raster scan was performed over the FOV at frame intervals of up to ~900 ms for 120

#179359 - $15.00 USD Received 6 Nov 2012; revised 17 Jan 2013; accepted 17 Jan 2013; published 22 Jan 2013

s. The FLIM system accumulates photons over all frames into time-resolved photon distributions, one distribution for each pixel, yielding a 256 x 256 x 256 data cube resolved in x, y, and t with high signal to noise ratio. We performed an additional 3x3 spatial pixel binning to obtain decay profiles with ~5000 photons. We regard this value as the approximate minimum number of photons required to perform our multiple-component lifetime fits, containing 2 constrained lifetimes and 2 free lifetimes and described in Subsections 2.3 and 3.2, at each pixel [30].

After collecting physiological baseline measurements, a time series of measurements over the same FOV was collected with 32 x 32 pixel resolution. Spatial resolution was sacrificed to decrease the time-point measurement interval for the time series to 2.5 s, enabling time-resolved FLIM measurements during metabolic manipulations. For each time-point measurement, the FOV was repeatedly raster scanned for 2.5 s. Each individual frame required ~50 ms. The software accumulated photons over all ~50 frames and temporally binned using the same $\Delta t \approx 50$ ps intervals. Each time series consisted of continuous time-point measurements acquired for 5 minutes. To minimize photobleaching, excitation intensity was reduced to yield photon count rates of approximately 50,000 counts per second for these time-resolved measurements. Fluorescence decay measurements were added over all pixels in the field of view. For a given time-point measurement, decay profiles were added with their two neighboring time points, yielding temporally smooth transient profiles. Each decay profile for each time point was comprised of 400,000 recorded photons. The total greatly exceeds the necessary amount for our fitting procedure, yielding more robust and temporally smooth profiles. These experiments constitute our global characterization of cerebral tissue's response to anoxia. Subsequent investigations will feature modified experimental protocols with pointwise measurements, enabling both high spatial and temporal resolution for characterizing more localized, cell-specific changes in cerebral metabolism.

2.3. Data analysis: instrument response function and lifetime fitting

As an initial step for each experiment, the lifetime calculation accuracy was verified, and simultaneously, the instrument response function (IRF) was computed, using FLIM measurements of dissolved NADH (0.5 mM in saline). Early attempts to characterize the IRF using second harmonic generation (SHG) of collagen and sucrose were confounded by mismatch in spectral properties [17,31]. The IRF in a two-photon microscope can be recorded by using SHG or Hyper-Rayleigh scattering [32]. Both methods deliver ultrafast signals at a wavelength detectable by the FLIM system. However, in contrast to fluorescence, most of the light is emitted in forward direction. The use of SHG may also require a change in laser wavelength. This can cause a shift in amplitude and phase of the timing reference pulses and thus a shift in the measured IRF. As NADH lifetime decay is well characterized [19,21] and its spectral features well match cytosolic and enzymatic bound NADH *in vivo*, NADH solution serves as a suitable reference emitter for evaluating these system characteristics under experimental conditions identical to our *in vivo* baseline measurements.

The IRF was computed using an iterative procedure. No a priori assumptions were made for the NADH decay parameters. For the first iteration, the decay portion of the experimental NADH solution measurement (from the peak time to the final time point, t_{final}) was fit as the sum of two decaying exponentials and a constant offset. A preliminary IRF was then computed by the expression

$$IRF(t) = FFT^{-1}\left(\frac{FFT\left(I_{measured}(t)\right)}{FFT\left(I_{theoretical}(t)\right)}\right), \tag{1}$$

where FFT and FFT^{-1} denote the Fast Fourier Transform and inverse Fast Fourier Transform, respectively. For each subsequent iteration the entire experimental decay curve of measured NADH solution (from $t = 0$ to t_{final}) and the computed $IRF(t)$ from the previous iteration were

#179359 - $15.00 USD Received 6 Nov 2012; revised 17 Jan 2013; accepted 17 Jan 2013; published 22 Jan 2013

used to compute coefficients for a new theoretical decay. The new theoretical profile was then used in Eq. (1) to re-compute $IRF(t)$. The procedure continued for 5 iterations. The decay coefficients yielded consistent values after the second iteration. The coefficients and $IRF(t)$ from the iteration yielding the smallest fitting error (reduced χ^2) were chosen.

The fluorescence decays measured from *in vivo* brain tissue were fit with the expressions

$$I_{theoretical}(t) = I_{offset} + \sum_{i=1}^{N} \alpha_i \exp\left(-\frac{t}{\tau_i}\right), \tag{2}$$

$$I_{model}(t) = IRF(t) \otimes \left(I_0 \delta(t) + I_{theoretical}(t)\right), \tag{3}$$

where N = 4, as described in Subsection 3.2, α_i and τ_i represent the amplitude and lifetime of component I, and I_{offset} represents the constant baseline intensity resultant from detector noise or ambient room light. $I_0\Delta(t)$ models the ultrafast signal component observed in the detected response. This component generally constitutes a miniscule amount of the detected response and its origin is not well understood. In our experiments, the ultrafast component likely arises from backscattered excitation light [19]. Generally, negligible amounts of excitation light penetrate through the emission filters and reach the detectors. However, in highly scattering tissue such as the brain, the contribution of the ultrashort excitation pulse should be accounted for and can be modeled as a Dirac delta function [19,33].

2.4 *In vivo* animal studies

Animals were prepared under a protocol approved by the Subcommittee on Research and Animal Care at Massachusetts General Hospital. As described previously [34] and illustrated in Fig. 1a (inset), cerebral cortices were exposed via a sealed cranial window in the skulls of anesthetized and ventilated Sprague Dawley rats (male, 195–265 g, Charles River). Cortical astrocytes were fluorescently labeled by topical application of sulforhodamine 101 dye (SR101, Sigma) [35]. Rats were initially anesthetized by isoflurane (1-2%). Following preparation under isoflurane, rats remained anesthetized and immobilized for the duration of the experiment with continuous infusion of alpha-chloralose (25 mg/kg/hr, Sigma Aldrich) and pancuronium bromide (2 mg/kg/hr, Hospira), respectively. Body temperature was monitored and controlled using a rectal temperature probe and heating blanket, respectively. The right femoral artery and vein were cannulated to monitor blood gases and pressure and to administer anesthetic. Using a flowmeter and a ventilator, gas fractions and inspiration rates were adjusted to maintain systemic blood gas and pH levels within physiologically normal range (pCO_2: 37 ± 5 mmHg, pO_2: 115 ± 15 mmHg, pH 7.39 ± 0.05). Brief periods of anoxia, not exceeding 45 s, were administered by respiratory arrest.

Reduction of inspired oxygen stimulates increases in cerebral blood flow and volume *in vivo*, resulting in a greater amount of hemoglobin throughout the cerebral vasculature. We corrected for the adverse influence of augmented hemoglobin absorption and obstructed excitation light using the SR101 transient profile and a correction algorithm published previously [34]. Only the SR101 intensity signal was required for the correction algorithm. For each time point, the intensity was computed as time integrated SR101 photon counts at each pixel. No FLIM fitting was performed on the SR101 data. To verify that SR101 does not interfere with NADH lifetime measurements, we imaged solutions of SR101 in saline. Although the detected SR101 intensity in channel 2 was comparable to that observed in our *in vivo* experiments, negligible amounts of SR101 fluorescence were detected in the NADH channel from SR101 solutions.

#179359 - $15.00 USD Received 6 Nov 2012; revised 17 Jan 2013; accepted 17 Jan 2013; published 22 Jan 2013

3. Results

3.1. FLIM measurements of NADH solution

The fluorescence decay profile of a pure NADH solution was modeled as a bi-exponential decay, in which the two terms reportedly account for different folding conformations of the molecule [19,36]. Using a nonlinear least squares algorithm [15], we consistently computed fluorescence lifetimes of 395 ± 10 ps and 1.05 ± 0.010 ns for the two components of NADH solution, with relative amplitudes of 90% and 10%, respectively. Though our observations yield an average lifetime similar to previous 2P microscopy characterizations of NADH solution (460 ps, compared to 444 ps [19] and 480 ps [21]), the computed lifetimes of the short and long components differ by 12.5% and 24% of reported results. The discrepancy may be attributable to different microenvironmental conditions such as solvent medium, temperature, pH, viscosity, or concentration.

3.2. In vivo measurements: baseline conditions

Figure 1b displays an autofluorescence intensity image of a cortical astrocyte *in vivo*, measured approximately 65 μm below the tissue surface. The astrocytes' processes appear relatively bright; however, the image appears diffuse and noisy due to the nonzero signal outside the cell. The extracellular intensity arises from NADH autofluorescence in the surrounding neuronal and astrocytic processes. Analyses of preliminary *in vivo* brain tissue experiments were performed with commercial software (SPCImage, Becker & Hickl GmbH). Attempts to fit baseline experimental *in vivo* data at each pixel (after 3x3 binning) as the sum of two or three decaying exponentials routinely indicated the presence of four distinct NADH components, illustrated in Fig. 1c and consistent with previous reports [19,37] that detail *in vitro* brain slice measurements and rat liver, as well as our own unpublished observations in brain slices. Each of the four components were found to be independently sensitive to metabolic perturbations such as varied fraction of inspired oxygen or application of potassium cyanide [unpublished results]. This motivated the development of custom lifetime-fitting software in Matlab for all subsequent data analysis.

From our early fitting computations, which computed all lifetimes and amplitudes, we observed that the first two components consistently yielded lifetime values close to 0.395 and 1.0 ns. This lead to the conclusion that the first two components (a) correspond to the different folding conformations of free NADH identified from our NADH solution measurements and (b) the lifetimes of these components remained the same between our NADH measurements in solution and those measured *in vivo*. Consequently, we modified our fitting routine such that τ_1 and τ_2 were constrained within ±10 ps of the lifetime values computed for NADH solution at the start of each experiment. A nonlinear least squares fitting routine was then used to compute I_0, τ_3, τ_4, and α_i for i = 1-4. Figure 1d illustrates example profiles of *in vivo* cerebral NADH fluorescence, including the $I_{measured}(t)$, $I_{model}(t)$, and $IRF(t)$, and the associated fit values computed with our custom software. Residual values multi-exponential fits containing 2, 3, and 4 components are displayed in Fig. 1e. A bi-exponential model was found to be inadequate to model *in vivo* NADH fluorescence lifetime, as indicated by the residual profile. While both 3- and 4-component models yielded more satisfactory residual profiles, the 4-component model consistently resulted in smaller fitting errors.

Figures 2a-2b display representative high-resolution intensity images of rat cortical tissue collected *in vivo* with our microscope, roughly 70 μm below the brain surface. Astrocytic cell bodies appear bright in the SR101 fluorescence images due to their preferential dye uptake over neurons [35]. Their processes envelop cerebral microvasculature, whose cross sections appear as dark circles in the intensity images. As shown in Fig. 2a, the SR101 intensity image permitted identification of astrocytic cell bodies (yellow) and blood vessels (red). We designated the remaining tissue as the neuropil, comprised primarily of processes from both neuronal dendrites and astrocytes. While select cell bodies appear brighter than the

#179359 - $15.00 USD Received 6 Nov 2012; revised 17 Jan 2013; accepted 17 Jan 2013; published 22 Jan 2013

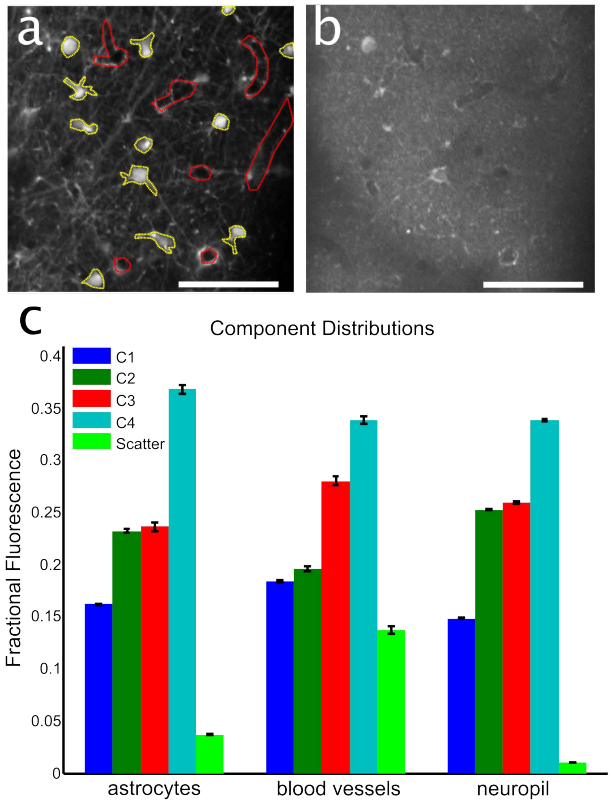

Fig. 2. Spatial distributions of cerebral NADH components *in vivo* (a-b) Example *in vivo* intensity images collected from the rat cortex, ~70 µm below the cortical surface. (a) SR101 fluorescence preferentially accumulates within astrocytic cell bodies and processes, enabling distinction between astrocytic cell bodies (yellow ROIs), blood vessels (red ROIs), and neuropil. (b) NADH fluorescence can be seen more uniformly throughout the tissue, though overlying vasculature results in shadows. (c) Distributions of fractional fluorescence for the four computed NADH components and purported scattering component, determined by fitting the fluorescence decays at each pixel and classifying pixels as astrocytes (yellow ROIs) blood vessels (red ROIs), or surrounding neuropil (scale bar: 50 µm, error bars: standard error)

background, NADH autofluorescence is generally ubiquitous within the tissue, allowing for little contrast of structural features at this magnification. As seen in the lower left corner, shadows of overlying blood vessels are visible as a result of obstructed focusing of excitation light by scattering red blood cells and from absorption of NADH emission by hemoglobin [34]. Figure 2c displays the tissue-specific fractional fluorescence of each NADH component, calculated at each pixel as

$$f_k = \frac{\alpha_k \tau_k}{\sum_{i=1}^{N} \alpha_i \tau_i}. \quad (4)$$

Figure 2c also shows the average amount of detected ultrafast signal in each tissue (I_o in Eq. (3), which we attribute to back-scattered excitation light, normalized to its overall maximal value. We observed that the NADH components generally appear heterogeneously distributed and diffuse across the tissue, and the components' spatial distributions do not coregister well with particular cellular structures seen in the SR101 intensity images. This phenomenon was observed in fractional fluorescence images computed with both our custom software and with commercial SPCImage software, used to calculate 2- and 3-component fits

#179359 - $15.00 USD Received 6 Nov 2012; revised 17 Jan 2013; accepted 17 Jan 2013; published 22 Jan 2013

[unpublished results]. The first NADH component (C1), which has the shortest lifetime (fixed at ~0.4 ns) and likely represents NADH unbound from any enzyme, constitutes a similar amount of the fractional fluorescence for astrocytes, blood vessels, and the neuropil. Its relative amplitude suggests that it is the most prevalent component. However, C1 makes the smallest contribution to the overall fluorescence signal due to its shorter lifetime. The lifetime of C2 was constrained to ~1 ns. Its computed relative amplitude was found to be less than that of C1 but greater than the other components. Its contribution to the fractional fluorescence was smaller in blood vessels compared to astrocytes and neuropil. C3 has a computed peak lifetime of 1.7 ns. This lifetime value corresponds well with a component observed in solutions of NADH bound to both malate dehydrogenase and lactate dehydrogenase [20,38]. C3 appears in similar amounts as C2 in both astrocytes and the neuropil, but it contributes considerably more than C2 to fractional fluorescence in the blood vessels. C4 has a peak lifetime value of 3.2 ns. In astrocytes, blood vessels, and neuropil, it has the greatest contribution to the fractional fluorescence, likely attributable to its longer lifetime. A component with similar lifetime and relative proportion has been observed in malignant and normal HS578 breast cells [20]. The contribution from backscattered excitation light is substantially higher in astrocytic cell bodies than the neuropil, and it is higher still in the blood vessels. This suggests that the back scattering in tissue arises primarily from cell bodies rather than dendritic processes.

Our baseline measurements consisted of multi-exponential lifetime fitting at each pixel using fluorescence profiles consisting of approximately 5000 photons. We consider 5000 to be the minimum number of photons required to perform rough lifetime fits using our method of constraining the first 2 of 4 lifetime values. Table 1 displays our modeling results for a theoretical decay consisting of 5000 photons with various added amounts of noise. The amplitude of the noise ranged between 0 and 200% of shot noise (the square root of the photon counts in each binning interval), and τ_1 and τ_2 were constrained within ± 10 ps. The mean and standard deviations are provided for the coefficients from a total of 10 trials for each noise amplitude.

In the presence of shot noise, the computed lifetime values were found to be reasonably stable, while computed amplitudes demonstrated more variability. Average lifetime values remained within 10% of the original value, and amplitudes varying by as much as ~35%. Adding twice as much noise yielded more variability, with up to 45% change in computed lifetime value and 65% change in amplitude. Under normal conditions, the noise component should remain well below twice the shot noise. Therefore, we believe analysis of profiles with 5000 photons is suitable for measuring rough but reasonably stable FLIM parameters.

Table 1. Computed parameters from profiles modeled with varied levels of added noise

	Original	+ 0.5x shot noise	+ 1x shot noise	+ 2x shot noise
α_1	73.42	72.57 ± 5.79	69.85 ± 6.83	76.08 ± 9.27
α_2	64.79	58.54 ± 20.81	69.79 ± 9.04	61.84 ± 26.50
α_3	18.22	26.23 ± 17.01	20.99 ± 6.86	35.41 ± 22.40
α_4	27.07	29.32 ± 3.09	28.82 ± 2.59	23.66 ± 11.58
τ_1	0.41	0.399 ± 0.01	0.40 ± 0.01	0.41 ± 0.01
τ_2	0.99	1.00 ± 0.01	0.99 ± 0.00	0.99 ± 0.01
τ_3	1.82	1.51 ± 0.23	1.67 ± 0.22	2.21 ± 0.90
τ_4	4.21	4.37 ± 0.22	4.62 ± 0.15	6.02 ± 2.12
I_{offset}	0.05	0.04 ± 0.01	0.04 ± 0.02	0.04 ± 0.02

3.3. In vivo measurements: anoxia transients

Figure 3a displays representative transient profiles of amplitude weighted lifetimes, $\alpha_i\tau_i$, *i:* 1-4_i, of the four NADH components during a brief period of anoxia, induced by respiratory arrest. The profiles were computed from decay profiles assembled over the entire field of view. The profiles have also been normalized to the average baseline value and corrected for

#179359 - $15.00 USD Received 6 Nov 2012; revised 17 Jan 2013; accepted 17 Jan 2013; published 22 Jan 2013

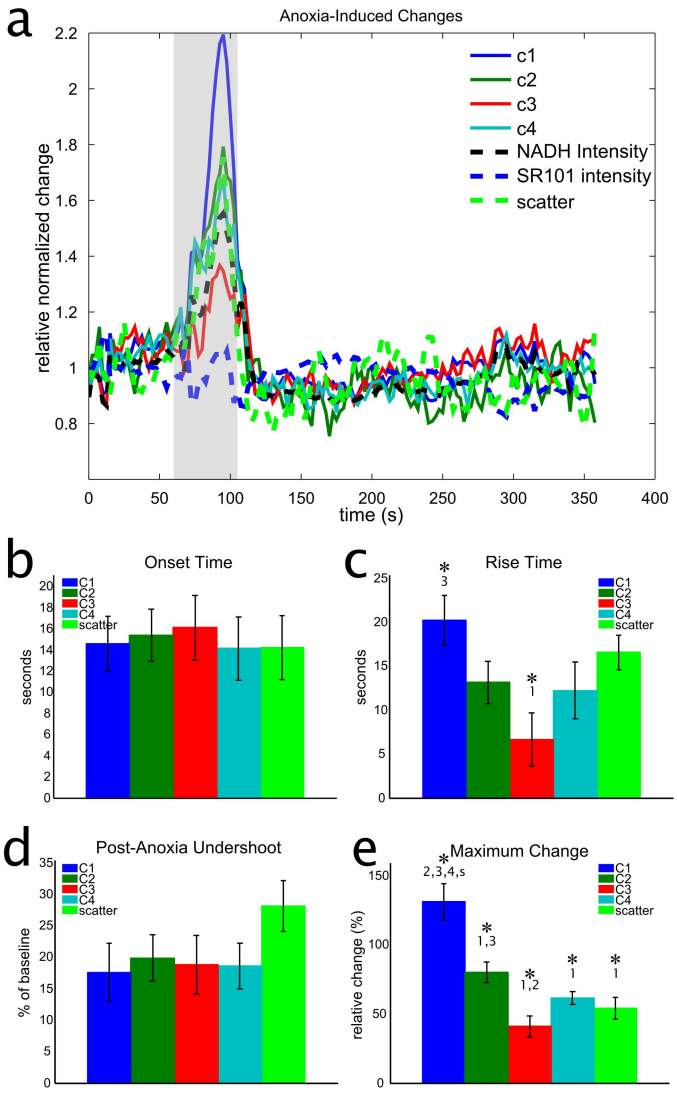

Fig. 3. NADH transients during anoxia (a) Representative global transients of NADH components (amplitude-weighted lifetime, $\alpha_i\tau_i$), and intensity transients for NADH, SR101, and backscattering. The shaded region corresponds to a 45 s period of anoxia, after which respiration was immediately restored. (b-e) Average component-specific changes in (b) anoxia-induced onset time (c) rise time (d) relative undershoot, and (e) maximal relative change, as measured from 10 trials of anoxia. Error bars denote standard error. * denote statistically significant differences from indicated components, measured with paired t-tests ($\alpha = 0.05$)

changes in blood volume and hemoglobin using the metabolically inert SR101 dye signal and a correction algorithm [34]. NADH intensity, SR101 intensity, and I_0 are also included. During the onset of anoxia, pronounced, steep rises are observed in all NADH components, NADH intensity, and $I_0(t)$ as halted oxygen supply progressively limits oxidative phosphorylation. Transient profiles were analyzed for 10 anoxia trials in a total of 7 rats, and results are provided in Figs. 3b-3e. In all trials, respiration was restored after 45 seconds. Arterial blood pressure dropped drastically from ~110 mmHg to ~50 mmHg during the anoxic episode, but quickly recovered during oxygen restoration. Onset time (t_{10}) and rise

#179359 - $15.00 USD Received 6 Nov 2012; revised 17 Jan 2013; accepted 17 Jan 2013; published 22 Jan 2013

time (t_{90}–t_{10}) were calculated from interpolated time courses (Δt = 0.1 s) by finding the times t_{10} and t_{90} required to increase from average baseline value to 10% and 90% of the maximum value, respectively. For all measured parameters, onset times occurred approximately 15 s after initiating respiratory arrest. Paired *t*-tests (α = 0.05) were performed for all measurements in all animals. Onset times and peak undershoot values were found not to be significantly different across the 4 NADH components or I_0. NADH components 1 and 3 had significantly different rise times, with component 3 rising nearly 3 times faster than component 1. Components 1, 2, and 3 all have significantly different maximal changes, with component 1 changing by nearly 2 and 3 times as much as components 2 and 3, respectively. I_0 represents the changes in magnitude of backscattered excitation light. Under hypoxic conditions, reports have suggested that increases in scattering can be attributed to mitochondrial swelling [19,39]. The observed transient profiles in the backscatter signal were found to correlate well with profiles of NADH component 4, with similar onset times, amplitude changes, and undershoots. While more rigorous investigation is required for validation, the correlation suggests that NADH component 4 may represent a formulation of NADH bound to a large mitochondrial enzyme, and could be a more specific indicator of changes in oxidative metabolism.

4. Discussion and conclusion

NADH fluorescence lifetime has been characterized in a wide range of biological samples and pathological conditions, including isolated mitochondria [33,37], *in vitro* cell cultures [20,22,29,37,39–41], *ex vivo* tissue [19,21,23,37,42], and *in vivo* measurements [23,43,44]. To our knowledge, we report the first observations of NADH lifetime using 2P microscopy in cerebral tissue *in vivo*. NADH fluorescence decays are typically modeled as the sum of multiple (2 – 4) decaying exponentials, representing different enzyme-bound formulations, (i.e. species [19]), with distinct lifetimes. Although the species with shortest lifetime is widely believed to indicate 'free' NADH, unbound from any enzyme, the total number of identifiable species, and their associated lifetimes and represented enzymatic processes, remains unresolved. NADH participates in numerous reactions of glycolysis, the Kreb's cycle, and oxidative phosphorylation. Several enzymes and proteins exist to which NADH can intermediately bind both in the cytosol and mitochondria. Therefore, practical models of multiple exponential decays necessarily represent an oversimplification of the underlying cellular metabolic processes [45]. Investigators have reported similarities in lifetime values between their intracellular NADH measurements and solutions of NADH complexed with isolated enzymes such as lactate dehydrogenase and malate dehydrogenase [19,20]. Together with mitochondrial complex I, it is likely that the observed NADH species reflect intermediate binding with these particular enzymes. However, more investigation is required, particularly to account for the differences in enzymatic activity and environmental conditions between solution medium and the intracellular environment.

Discrepancies in the number of components and lifetime values exist between our observations and published values. As one of several examples, Niesner et al. reported a distribution of NADH lifetimes suggesting the presence of only 2 components, representing unbound and "protein-bound" NADH, observed in cultured dermal fibroblasts [18]. The discrepancies between our observations and those of Niesner et al. and others may be attributable to several different experimental parameters and conditions utilized in each study. In particular, the different cell types, investigated primarily under *in vitro* and *ex vivo* conditions, and different computational methods would likely account for most of the discrepancies. To our knowledge, we report the first *in vivo* FLIM observations of NADH in the rodent cerebral cortex. Under these *in vivo* conditions, we monitored the metabolic activity of more than one cell type (neurons, astrocytes, vascular endothelial cells, etc), and the supply of oxygen and other metabolites are likely more spatially heterogenous than under cell culture or brain slice conditions [24,46]. Niesner et al. observed that the weighted

#179359 - $15.00 USD Received 6 Nov 2012; revised 17 Jan 2013; accepted 17 Jan 2013; published 22 Jan 2013

averages of NADH lifetimes in dermal fibroblasts differ from those measured in solution, and they suggested that the differences are attributable to the variations in microenvironmental conditions such as viscosity, pH, and refractive index. These environmental differences would likely be more pronounced and heterogeneous under *in vivo* conditions, and this may explain why our lifetime distribution in Fig. 1c differs markedly from their distribution. Additionally, they utilized the noniterative Prony method rather than the nonlinear least squares method to calculate their lifetimes, which also could contribute to the difference. Our observation of 4 NADH components is consistent with the results of Vishwasrao et al. [19], but it differs from those of Chia et al. [21]. Both investigators measured NADH lifetime in hippocampal slices of Sprague Dawley rats. Compared to our results, Chia et al. performed analysis on traces with fewer photon counts (~1200), and utilized the commercial SPCIMage software, which can perform fits with a maximum of 3 components. This may account for the differences in our results.

Like NADH, another important electron carrier for oxidative metabolism, flavin adenine dinucleotide (FAD), is also autofluorescent, but in its oxidized form. In principle increased FAD fluorescence suggests an increase in oxidative phosphorylation via succinate dehydrogenase (mitochondrial complex II) [7]. Simultaneous detection of reduced NADH and oxidized FAD fluorescence enables calculation of the redox ratio, a semi-quantitative measure of energy respiration and the oxidation-reduction state in the mitochondrial matrix that is independent of the factors influencing the fluorescence measurements [22,47–49]. FAD measurements are reportedly limited by low signal, spectral overlap with other endogenous fluorophores such as lipofuscin [50], and less responsiveness to metabolic perturbations [51]. Efforts are currently underway to address these limitations and collect robust 2P *in vivo* FLIM measurements of FAD in channel 2 of our system.

Our *in vivo* observations suggest the existence of a minimum of 4 distinct, detectable species in brain tissue. This motivated us to evaluate the lifetime data using a 'quasi-global' analysis method, where profiles were fit to a 4-component multi-exponential fit, with 2 lifetimes held constrained to those measured in NADH solution, our designated reference emitter [17,52]. Further, rigorous investigation is required to identify which metabolic enzymes and proteins could be represented by each specie. In order to monitor shifts in glycolytic and oxidative metabolism, however, this level of detail may not be necessary. It may be sufficient to associate the species with different metabolic reactions without identifying its associated enzyme. Future investigations will explore the viability of this technique by monitoring transient features of each component during exposure to various metabolic inhibitors.

Our identification of 4 distinct components agrees well with reported *ex vivo* brain tissue and isolated liver mitochondria measurements [19,37]. Though the physical significance of parameters derived from a 4-component exponential fit has been disputed [53], our hypothesis is supported by the observation that each component responds differently to metabolic perturbations. For our baseline *in vivo* measurements, we performed rough multi-exponential lifetime fits with high spatial resolution. Fits were performed at each pixel on profiles with ~5000 photons, after 3 x 3 binning. Modeling results also showed that calculated lifetime parameters were reasonably stable for simulated fluorescence decays with ~5000 photons and added shot noise. Published values for the minimum number of photons required for precise resolution of 2 free lifetime components range from 1000 to 400,000 [30,54]. Although Köllner and Wolfrum theoretically calculated that 400,000 photons are needed to determine the components of a double-exponential decay [54], it should be noted that they used an example of an extremely unfavorable composition of the decay (10% of 2 ns and 90% of 4 ns). In practice, the chance of resolving a multi-exponential decay function into its components dramatically increases with the ratios of the component lifetimes, and with the amplitude(s) of the fast components. For the typical decay composition of NADH, we obtained reasonably stable parameters by fitting decay functions containing approximately

#179359 - $15.00 USD Received 6 Nov 2012; revised 17 Jan 2013; accepted 17 Jan 2013; published 22 Jan 2013

5000 photons. We therefore consider 5000 as the minimum number of photons required to perform our multiple-component lifetime fits, containing 2 constrained lifetimes and 2 free lifetimes. This minimum photon threshold, coupled with 3 x 3 spatial binning, was determined to be the best compromise between spatial resolution and SNR, and yielded consistent lifetime values across measurements. Nevertheless, the low 2P cross section of NADH [12] limits signal for 2P FLIM measurements using TCSPC. This, in turn, reduces the precision for performing multi-exponential fits for each pixel and limits the ability to precisely measure the distributions of multiple NADH components in cytosol and individual mitochondria *in vivo*. In principle, collecting more photons, using either higher excitation intensity, longer dwell times, or longer scanning duration could enable fits with greater certainty [53]. However, great care must be taken to prevent photobleaching.

In contrast to previous reports [20,21], we did not observe punctate clusters of fluorescence in our lifetime images. Though their spatial distributions were heterogeneously distributed, fluorescence signals of each component could generally not be registered with distinct cellular structures. Instead, the fractional fluorescence images for our calculated components appear diffusely distributed. Our results likely differ from previous reports because we imaged with lower spatial resolution and a larger FOV. Imaging with a larger FOV is necessary for evaluating the complex metabolic interactions between different cell types associated with neurovascular coupling. Additionally, punctate intracellular features could also be blurred by potential motion artifacts associated with respiration during *in vivo* imaging.

The amount of fractional fluorescence intensity from each NADH component differs subtly between astrocytic cell bodies, blood vessels, and neuropil, as does the amount of back-scattered excitation light. C3 and C4 are believed to represent NADH bound to mitochondrial enzymes, and they contribute most strongly to fluorescence in all tissue types. Erythrocytes are the primary cell type in blood and lack mitochondria. The prevalence of C3 and C4 in blood vessels is therefore an unexpected observation. This finding requires more investigation, but the detected C3 and C4 could have been measured from other more metabolically active blood cells that contain mitochondria, such as macrophages and platelets. Blood vessels also scatter considerably more excitation light than astrocytes or neuropil. This could imply that the erythrocyte membranes have higher scattering properties than brain tissue.

Due to its spectral compatibility, measuring a solution of NADH and fitting to a 2-component model proved to be a more reliable method to determine the IRF compared to SHG measurement of collagen or sucrose. We employed methods of the global analysis technique [16] by constraining the first 2 lifetime values in our *in vivo* data fits, yielding robust 4-component fits of NADH lifetime in the cerebral cortex. We believe that constraining the values of the first two components is intuitive and practical. While other microenvironmental factors such as temperature and viscosity influence the lifetime value, it is reasonable to expect that enzymatic binding has the biggest influence on NADH. Therefore, in our fitting routine, restricting the upper and lower bounds of components 1 and 2 within 10 ps of the measurement grants the flexibility for these other factors while asserting that they correspond to distinct conformations of free NADH.

For our measurements of *in vivo* metabolic transients, we performed precise multi-exponential lifetime fits with lower spatial resolution, a suitable approach for investigating global phenomena such as anoxia. Under normal physiological conditions, the brain is supplied with a surplus of oxygen. Our observations show that, under our experimental conditions, only ~15 s of respiratory arrest is sufficient to deplete vascular oxygen supply to levels where oxidative phosphorylation rates start to diminish in the rat cerebral cortex. After this point, all observable NADH species increase sharply, as does tissue backscattering. The increase in scattering is believed to arise from mitochondrial swelling. However, it could also be attributable in part to anoxia-induced increases blood flow and hematocrit. Onset times for

#179359 - $15.00 USD Received 6 Nov 2012; revised 17 Jan 2013; accepted 17 Jan 2013; published 22 Jan 2013

these changes were found to be similar for all species and backscattering. However, the shortest lifetime component, which is believed to indicate unbound NADH, has the most pronounced increase. Kinetic features of the longest lifetime component are strikingly similar to those of tissue scattering, suggesting that this enzymatic formulation of NADH may be involved in the same metabolic process that induces mitochondrial swelling. These analyses over the entire FOV motivate further modifications to our technique to enable spatially resolved measurements with high temporal resolution. Future investigations will include point-wise measurements of fluorescence lifetime and anisotropy at designated locations in the field of view, enabling distinction of cell-specific responses to metabolic perturbations in the cortex.

Acknowledgments

This work was supported by NIH R01-NS057476, P50-NS010828, and P01-NS055104, R01-EB000790 and AHA 11SDG7600037. We gratefully acknowledge Boston Electronics for their generous support with the TCSPC equipment and software. Dr. Becker has a financial interest in Becker & Hickl GmbH, which did not support this work.

#179359 - $15.00 USD Received 6 Nov 2012; revised 17 Jan 2013; accepted 17 Jan 2013; published 22 Jan 2013